RESEARCH ARTICLE

ADVANCED MATERIALS
www.advmat.de

Incipient Ionic Conductors: Ion-Constrained Lattices Achieving Superionic-Like Thermal Conductivity Through Extreme Anharmonicity

Yongheng Li, Qiuchun Lu, Bin Wei, Cong Lu, Xingang Jiang, Taishun Manjo, Daisuke Ishikawa, Caofeng Pan,* Alfred Q. R. Baron, and Jiawang Hong**

Phonon liquid-like thermal conduction in the solid state enables superionic conductors to serve as efficient thermoelectric device candidates. While liquid-like motion of ions effectively suppresses thermal conductivity (κ), their high mobility concurrently triggers material degradation due to undesirable ion migration and consequent metal deposition, making it a challenge to balance low κ and high stability. Here, phonon liquid-like thermal transport is reported alongside restricted long-range ion migration in $CsCu_2I_3$ with incipient ionic conduction, using synchrotron X-ray diffraction, inelastic X-ray scattering, and machine-learning potential-based simulations. The Cu ions are revealed to exhibit confined migration between CuI_4 tetrahedra at high temperatures, displaying extreme anharmonicity of dominated phonons beyond conventional rattling and comparable to that in superionic conductors. Consequently, a glass-like κ (≈0.3 W m^{-1} K^{-1} at 300 K) following the relationship of $\kappa \approx T^{0.17}$, is achieved along the *x*-direction, where Cu ion migration is three orders of magnitude lower than in superionic conductors. These results highlight the advantage of incipient ionic conductors in simultaneously maintaining both low κ and high stability, elucidating the thermal transport mechanism via ion migration constraints, and paving an effective pathway toward ultralow thermal conductivity in ionic conductors.

1. Introduction

Low thermal conductivity, κ, is of special interest and highly desirable in thermal insulation, thermodiodes, and thermoelectrics, etc., but it cannot be arbitrarily low due to the intrinsic limitation by atomic vibrations in most semiconductors and insulators.[1,2] To overcome this issue intrinsically in materials such as thermoelectric, substantial progress has been made to suppress phonon propagation via structural design strategies from "phonon-glass" to "phonon-liquid."[3] Superionic conductors, by exploiting the liquid-like transport of phonons, have successfully realized such concepts, achieving exceptionally low κ to a glass limit in the solid state. For example, in Cu_2Se, the random distribution of Cu ions allows them to migrate freely, resulting in strong scattering of phonons and thus low κ (<0.5 W m^{-1} K^{-1}) over a wide temperature range.[4] In $CuCrSe_2$, specific phonons dominated by Cu ions break

---

Y. Li, X. Jiang, J. Hong
School of Aerospace Engineering
Beijing Institute of Technology
Beijing 100081, China
E-mail: hongjw@bit.edu.cn

Q. Lu
School of Materials Science and Engineering
Nanyang Technological University
639798, Singapore, Singapore

B. Wei
School of Materials Science and Engineering
Henan Polytechnic University
Jiaozuo 454000, China
E-mail: binwei@hpu.edu.cn

C. Lu
Multi-disciplinary Research Division
Institute of High Energy Physics
Chinese Academy of Sciences
Beijing 100049, China

T. Manjo, D. Ishikawa, A. Q. R. Baron
Japan Synchrotron Radiation Research Institute (JASRI)
SPring-8, Hyogo 679–5198, Japan

T. Manjo, D. Ishikawa, A. Q. R. Baron
Materials Dynamics Laboratory
RIKEN SPring-8 Center
RIKEN, 1-1-1 Kouto, Sayo, Hyogo 679–5148, Japan

C. Pan
Institute of Atomic Manufacturing
Beihang University
Beijing 100191, China
E-mail: pancaofeng@buaa.edu.cn

The ORCID identification number(s) for the author(s) of this article can be found under https://doi.org/10.1002/adma.202513381

DOI: 10.1002/adma.202513381

down due to giant anharmonicity and disorder, yielding low κ (< 1 W m^{-1} K^{-1}).[5] In Ag_8SnSe_6, mobile Ag ions with high mobility ($\sigma \approx 0.1$–10 S m^{-1}) dominate overdamped phonons, revealing extreme anharmonicity, responsible for low κ (< 0.5 W m^{-1} K^{-1}) and fast diffusion.[6] However, superionic conductors suffer from material degradation under operating conditions due to major ion migration and metal decomposition caused by electric fields or thermal gradients, hindering their practical application.[7] Thus, outstanding questions arising from such an issue remain on how to suppress ion migration to realize high stability while maintaining liquid-like thermal conductivity in ionic conductors.

Recent studies have proposed the concept of incipient ionic conductors, materials poised at the threshold of ionic conduction, where ions exhibit substantial local mobility yet experience suppressed long-range diffusion due to structural confinement within the host lattice.[8] This unique state bridges conventional electrical and typical superionic conductors, where collective ion motions have a certain impact on heat transfer without long-range displacement. As observed in tetrahedrite $Cu_{12}Sb_4S_{13}$, Cu ions are confined to migrate (low mobility) only between the corners of a given $SCu(2)_6$ octahedra, which is beyond rattling and yields a low κ (<1 W m^{-1} K^{-1}) even in the pristine system with crystalline stability.[8,9] As discussed above, the heat transport mechanisms are significantly different in superionic conductors, such as ionic diffusion induced phonon (selectively) broken down in $Ag(Cu)CrSe_2$,[5,10] extreme phonon anharmonicity in Ag_8SnSe_6,[6] and no ionic/phonon conductivity correlation in Ag Argyrodites.[11] Inspired by this, seeking new systems with constrained ionic migration is crucial to further validate the incipiency, ultimately revealing the fundamental link between lattice dynamics, thermal transport, and ionic transport in confined frameworks.

Possessing soft lattice structure and element synergy effect, ternary metal halides have been recently reported to suggest their potential for thermoelectric applications due to the ultralow κ and tunable electronic properties.[12] In alkali-metal halides containing Cu and Ag, $(AX)_x$–$(MX)_{1-x}$ (A = Cu/Ag, M = K/Rb/Cs, and X = Cl/Br/I), the halide polyhedral framework enables certain freedom of Cu/Ag to large motion, resulting in relatively low ionic conductivity ($\sigma < 10^{-6}$ S m^{-1} at room temperature), making them appropriate candidates for studing incipient ionic behavior in thermal transport.[13] Here, we selected $CsCu_2I_3$ as a demo to investigate this issue through a combination of synchrotron X-ray diffraction, inelastic X-ray scattering, and machine-learning potential-based molecular dynamics (MD) simulations. We reveal that the migration of Cu ions is predominantly confined to the approximate x-direction via an exchange mechanism between neighboring CuI_4 tetrahedra. This restricted ionic motion goes beyond the conventional rattling behavior and induces strong lattice anharmonicity, leading to the glass-like κ ($\kappa \approx 0.3$ W m^{-1} K^{-1} at 300 K). Notably, the increase in thermal conductivity at high temperatures remains minimal, suggesting the mobility of ions has a limited impact on thermal transport. This work not only establishes halide compounds as a promising platform for incipient ionic transport but also offers a novel design strategy for achieving extremely low thermal conductivity.

2. Results and Discussion

2.1. Constrained Migration of Cu Ions

High-resolution single crystal synchrotron X-ray diffraction (SCSXRD) data were collected at beamline BL02B1 (SPring-8) to probe the temperature-dependent structural evolution of $CsCu_2I_3$, detailed in Supporting Information Figure S1 and Tables S1–S3 (Supporting Information). As illustrated in **Figure 1a**, the 300 K crystal structure adopts orthorhombic symmetry (space group *Cmcm*), where Cu ions occupy interstitial sites within an I anion tetrahedral sublattice, forming discrete CuI_4 units. These paired CuI_4 strings are confined within rhombic columnar cages of Cs cations and extend infinitely through edge-sharing, constituting the characteristic Cu_2I_3 chains. Structure factors extracted from SCSXRD enable the calculation of the maximum-entropy method (MEM),[14,15] which reconstructs probable electron density (ED) distributions, providing a robust approach for analyzing atomic localization,[16] disorder,[17,18] and ion migration intermediate (MID) pathways.[19] Figure 1b reveals localized ED peaks at adjacent Cu sites below 450 K, whereas a continuous diffusion channel emerges at 500 K, evidenced by connected ED maxima along MID in normalized profiles (Figure 1c). This channel suggests possible Cu ion diffusion or hopping between neighboring sites above 300 K. However, the low ED intensity within the channel (maximum ED < ≈4% of Cu-site peaks) indicates restricted ion mobility. Consequently, $CsCu_2I_3$ can be classified as an incipient ionic conductor with thermally activated yet kinetically limited ion transport.

Machine-learning potential-based MD simulations reveal Cu ion hopping dynamics at elevated temperatures (Figure 1d; Figure S2, Supporting Information). At 300 K, trajectories exhibit spherical confinement, whereas anisotropic displacements emerge at 450 K, manifesting as tentacle-like extensions from the spherical profile. The observed geometry shows broader Cu^+ displacement amplitudes at 450 K versus 300 K, and occasional Cu ion hopping occurs at 450 K. Upon heating to 600 K, more explicit ion hopping events occur with 3D characteristics: trajectories extend not only within the xy-plane but also sometimes along the z-direction, as visualized in the xz-plane projection (Figure 1e; Figure S2b, Supporting Information). This behavior aligns with the continuous ED channels (Figure 1b,c). The hopping mechanism primarily involves exchange processes between adjacent CuI_4 tetrahedra as yellow arrows in Figure 1e. Energy barrier simulations further elucidate this phenomenon (Figure 1f). The migration barrier along the MID pathway (0.12 eV) is

---

B. Wei
Anhui Province Key Laboratory of Intelligent Computing and Applications
Huaibei Normal University
Huaibei 235000, China

J. Hong
State Key Laboratory of Environment Characteristics and Effects for Near-space
Beijing Institute of Technology
Beijing 100081, China

J. Hong
Beijing Institute of Technology
Zhuhai, Guangdong 519088, China

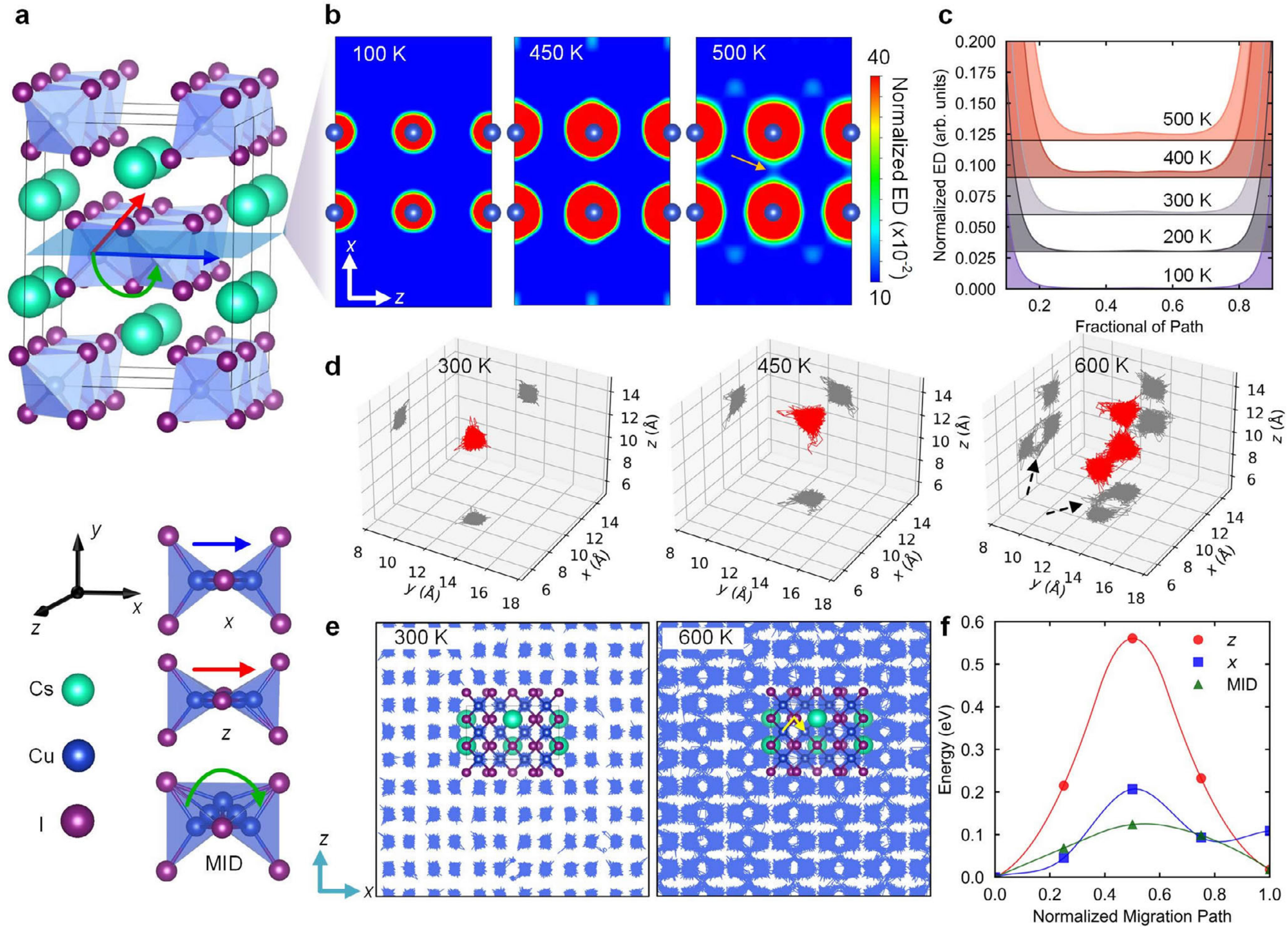

Figure 1. Temperature-driven motion of Cu ions in $CsCu_2I_3$. a) Crytal structure of $CsCu_2I_3$ with the (010) plane shadowed in light blue and migration pathways of Cu ions along *x*- ([100]), *z*- ([001]), and intermediate (MID) directions indicated by blue, red, and green arrows, respectively. b) Normalized electron density (ED) maps on the (010) plane from structure factors measured by single crystal synchrotron X-ray diffraction at 100, 450, and 500 K. The orange arrow indicates the delocalization of Cu ions at 500 K. c) Normalized ED profile through the MID pathways marked with green arrows in (a) with increasing temperature. d) Trajectories of selected single Cu ions from molecular dynamics (MD) simulation at 300, 450, and 600 K, showing the exchange of Cu ions across neighboring sites, as intuitively exhibited by extended trajectories in the *xz*-plane at 300 K and 600 K (yellow arrow in e). f) Calculated energy barrier along *x*-, *z*-, and MID-directions.

significantly lower than along the *z*-direction (0.56 eV) or *x*-direction (0.21 eV). These energy barrier simulations explain: 1) the formation of continuous energy density (ED) channels specifically along minimum ion diffusion (MID) pathways, 2) the primary ion migration pathway occurring through the exchange of Cu ions between nearest-neighbor CuI_4 tetrahedra, and 3) the relatively infrequent direct inter-tetrahedral hopping along Cartesian axes.

Cu ion hopping dynamics can be characterized by time-dependent mean square displacement (MSD) analysis (**Figure 2a**). At 300K, MSD of Cu^+ remains temporally invariant, indicating localized oscillations with a relatively large amplitude of ≈1 Å. As the temperature increases to 600 K, the MSD exhibits a nearly linear variation with time, signaling frequent inter-tetrahedral hopping between adjacent CuI_4 units. A projected time-resolved displacement trajectories further confirm the constrained hopping of a selected Cu ion: at 300 and 450 K, the selected Cu ion oscillates near equilibrium positions along Cartesian axes. At 600 K, hopping to adjacent CuI_4 tetrahedra occurs with directional preference—the hopping frequency along the *x*-direction exceeds that along the *z*-direction, and along the *y*-direction exhibits only oscillation (no hopping) (Figure 2b vs Figure S3, Supporting Information). The ionic diffusion coefficient with high anisotropy agrees well with this directional preference of Cu ions (Figure 2c). Diffusivities along all axes approach zero at 300 and 450 K. At 600 K, the *x*-direction diffusivity is 9.3×10^{-8} cm^2 s^{-1}, while *z*-direction diffusivity reaches 2.0×10^{-9} cm^2 s^{-1}— an order of magnitude lower than *x*-direction. The *y*-direction diffusivity remains negligible ($< 10^{-9}$ cm^2 s^{-1}). Notably, hopping is restricted to the nearest-neighbor tetrahedral exchanges, with only a small probability of sequential hops to next-nearest sites, indicating suppressed long-range diffusion. This constraint is remarkable by compared with other superionic conductors, such as 1×10^{-5} cm^2 s^{-1} at 600 K in $AgCrSe_2$,[20] 1.3×10^{-5} cm^2 s^{-1} at 500 K in Cu_7PS_6.[21] These results demonstrate an excellent agreement with the suppressed

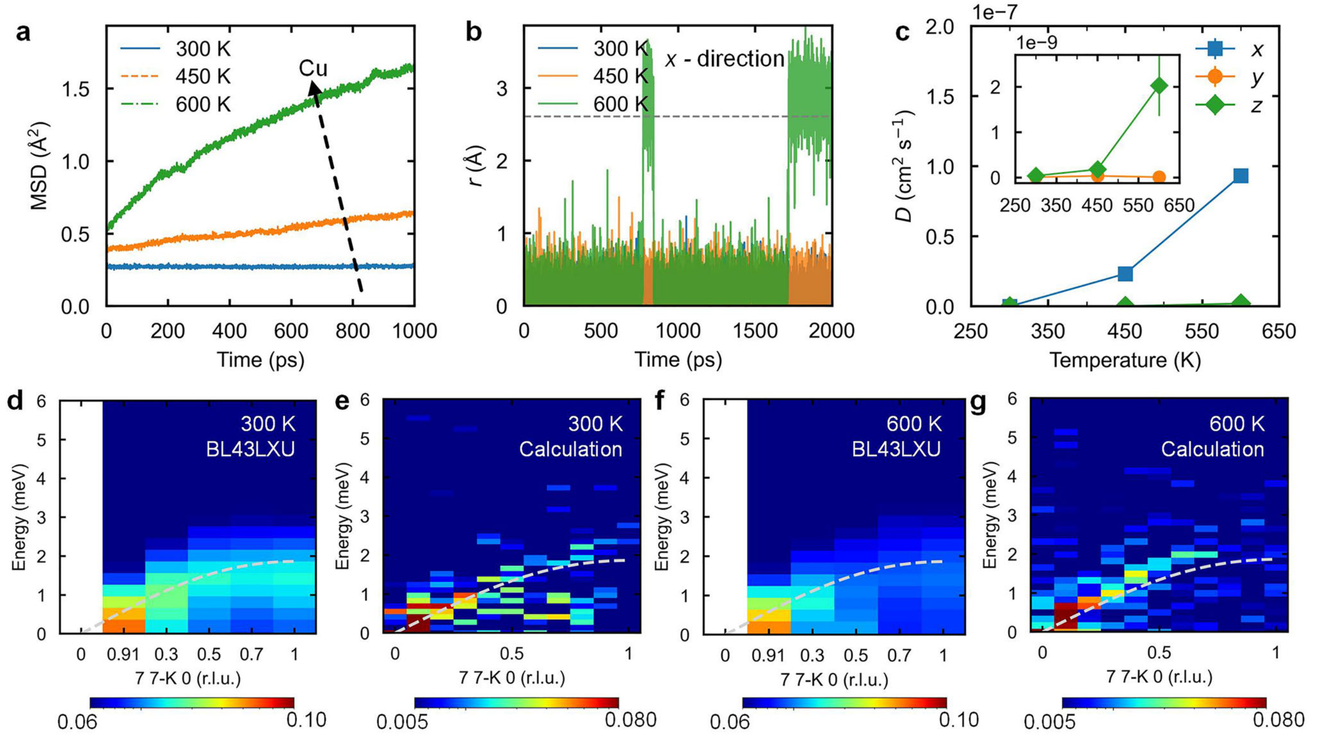

Figure 2. Hopping of Cu ions and well-defined phonons in $CsCu_2I_3$. Mean square displacements (MSD) of Cu ions at different temperatures from MD simulations. b) Time-dependent displacement of a selected Cu ion along the *x*-direction from MD. The grey dashed line indicates the distance between the nearest-neighboring CuI_4 tetrahedra. c) Diffusion coefficient of Cu ions along different directions at different temperatures. The inset shows an enlarged view of the diffusivity between 0 and 2.5×10^{-9} cm^2 s^{-1}, illustrating diffusivity along the *y*- and *z-directions*. d,f) are measured phonon dispersion along the [0 -K 0] direction at Q = (7 7 0), while e,g) are simulated phonon dispersion along the same direction at Q = (7 7 0) at 300 K and 600 K, respectively. The dashed lines in (d-g) are calculated TA branch at 300 K. The colorbar represents the intensity on a logarithmic scale.

long-range ionic diffusion and previously reported low ionic conductivity,[13] suggesting $CsCu_2I_3$ to serve as an appropriate incipient ionic conductor.

2.2. Cu Ion Dynamics Beyond Rattling Inducing Extreme Phonon Anharmonicity

Figure 2d–g shows the measured phonon dispersions along Γ−Y (*y*) direction at 300 and 600 K by inelastic X-ray scattering (IXS) at beamline BL43LXU (SPring-8),[22–24] which are well reproduced by our simulation. The discrepancies in the intensity distribution may arise from the use of smoothing functions and the omission of the resolution function in the calculations. Importantly, the transverse acoustic (TA) branch, typically employed to assess ionic diffusion, persists at elevated temperatures despite Cu ion hopping that drives the system beyond rattling dynamics. Although increased diffusivity is observed near the zone boundary at 600 K (attributable to thermally enhanced anharmonicity), the TA modes remain well-defined. Identical behavior is confirmed along Γ−X and Γ−Z directions (Figure S4, Supporting Information), demonstrating thermal robustness. This phenomenon arises from constrained Cu ion migration, where the residence time (τ) at each site substantially exceeds the phonon oscillation period.[25] Consequently, TA phonons demonstrate crystalline-like propagation behavior, which is a characteristic signature of incipient ionic conductors.

Figure 3a–c demonstrates good agreement between measured phonon dispersions and our simulation. Figure S5a (Supporting Information) indicates that phonon mode ≈4 meV are closely related to the vibration of Cu atoms. While TA modes remain well-defined at elevated temperatures, most optical modes (4–6 meV) exhibit substantial broadening. Some of them even become overdamped, as confirmed by the constant-**Q** scans depicted in Figure 3d–f. Notably, even TA modes at 300 K show slowly decaying intensity profiles with characteristic tails, often featuring shoulders corresponding to optical modes. These optical peaks broaden significantly and eventually vanish at 600 K (Figure 3d–f), indicative of overdamping. This overdamping directly correlates with Cu ion dynamics, as evidenced in Figure 3a–c,g–i and S6 (Supporting Information). Cs atoms also contribute to the anharmonicity as "rattler" but most of them are located above 4 meV, while Cu atoms contribute to the flat optical phonon bands around 4 meV (Figure S5, Supporting Information). The density of states (DOS) evolution reveals that discrete peaks between 4–6 meV at 300 K coalesce into a broad feature at 600 K. Projected partial DOS analysis attributes this primarily to Cu atoms: while Cs ions (rattler) exhibit minimal temperature-dependent DOS changes near 4 meV (Figure S6a, Supporting Information), and I ions show small variations (Figure S6b,c, Supporting Information), Cu-related peaks within

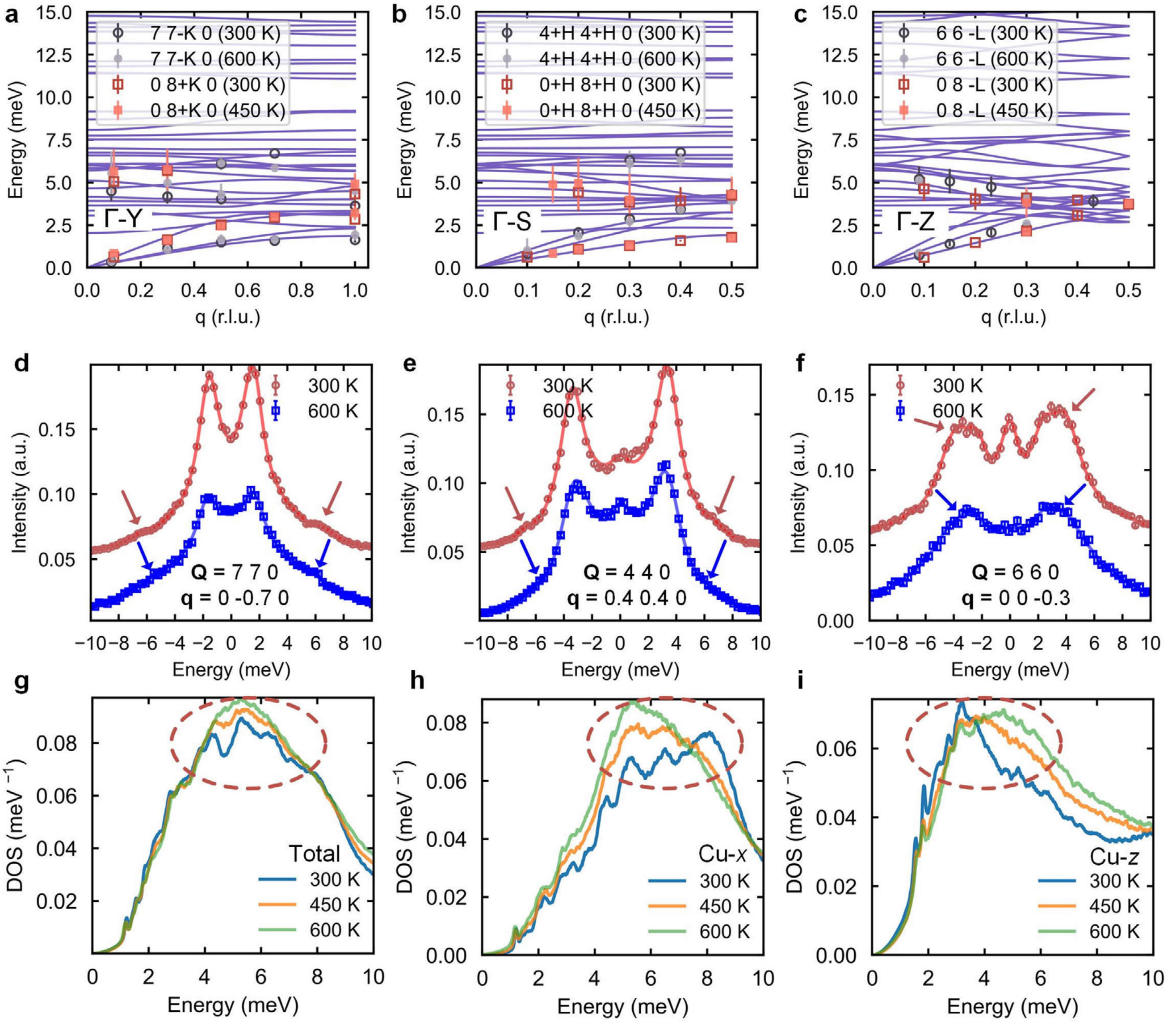

Figure 3. Phonon dispersion and density of states in $CsCu_2I_3$. a–c) are measured phonon dispersion by inelastic X-ray scattering (IXS) along the Γ−Y, Γ−S, and Γ−Z, respectively, overlaid with the calculated phonon dispersion at 300 K. Hollow markers, solid squares, and solid circles represent results at 300, 450, and 600 K. Error bar indicates the phonon linewidth. d–f) are experimental constant-Q scans at Q = (7, 6.3, 0), (4.4, 4.4, 0), and (6, 6, −0.3), respectively. Solid lines are fitting curves. (g) is simulated total phonon density of states (DOS), (h-i) are simualted *x*-directional and *z*-directional projected DOS of Cu at different temperatures. Dashed circles indicate the Cu-dominated peak merging with increasing temperature.

4–6 meV disappear completely with heating, indicating contributes most to the disappearance of total DOS peaks within 4–6 meV in Figure 3g. As mentioned above, Cu ion hopping is directionally oriented. The dynamics of Cu ions, extending beyond rattling behavior, result in a distinct temperature-dependent evolution of DOS along different directions. As evidenced in Figure 3h–I and Figure S6d–f (Supporting Information), DOS of Cu along the *x*-direction exhibits the most pronounced DOS changes upon heating, followed by that along the *y*-direction. Along the *z*-direction, peaks broaden without disappearance at higher temperatures. This directional preference aligns with preferential hopping along the *xy*-plane MID pathway, while *z*-direction migration remains infrequent. Crucially, the broadened 4–6 meV peaks at elevated temperatures are closely related to optical modes exhibiting large phonon linewidths and overdamping (Figure 3d).

We can now confirm that the “beyond rattling” behavior of Cu ions significantly influences phonon properties in $CsCu_2I_3$. As shown in Figure 2b, Cu ions primarily exhibit high-frequency vibrations with displacements of ≈1 Å, characteristic of a rattling state, interspersed with occasional hopping. This distinctive “beyond rattling” behavior drives two key effects: first, it leads to flat and even overdamped optical phonon bands, as demonstrated by the calculated phonon dispersions in Figure 3a–f and S5a (Supporting Information), accompanied by extreme anharmonicity; second, Cu ion migration markedly affects the phonon

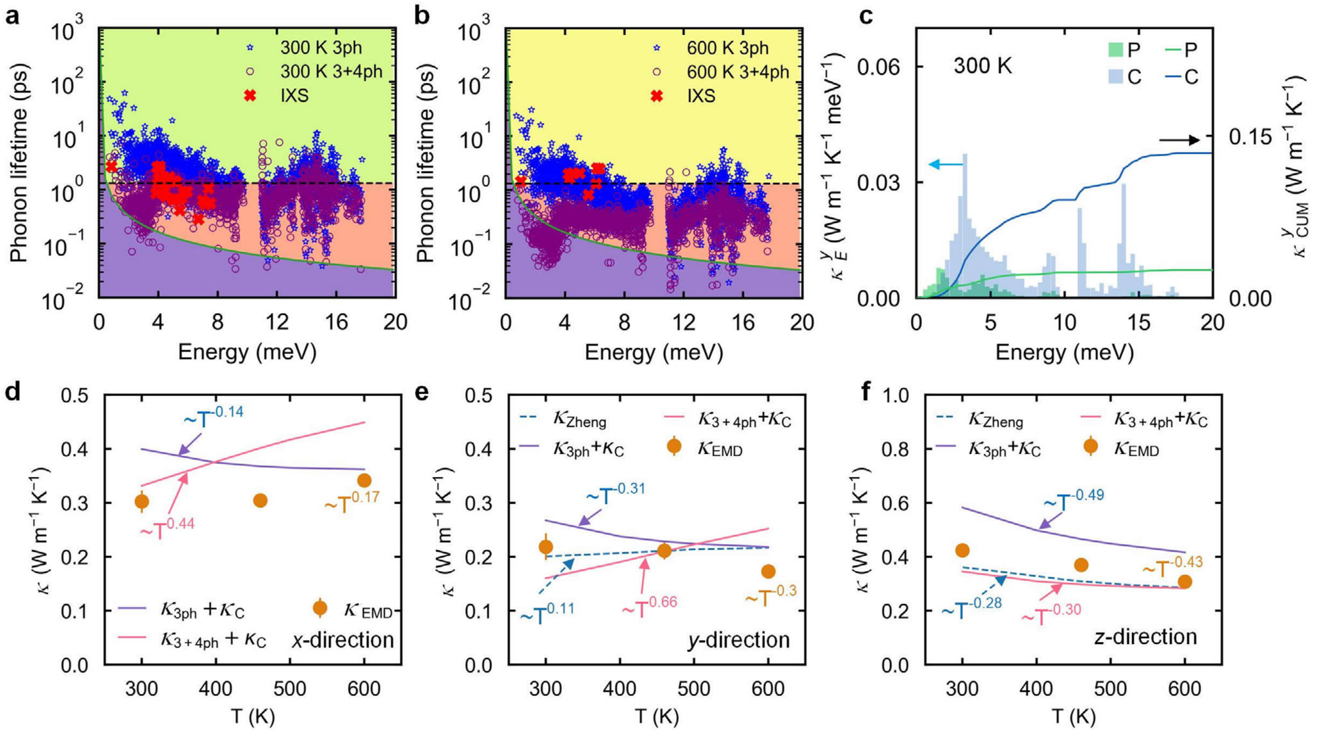

Figure 4. Phonon lifetime and thermal conductivity of $CsCu_2I_3$. a,b) are the calculated energy-dependent phonon lifetimes at 300 and 600 K. Blue stars and purple circles are the results of three-phonon (3ph) and that considering four-phonon (3+4ph), respectively. The red crosses are measured by inelastic X-ray scattering (IXS). The black dashed line represents the Wigner limit $1/\Delta\omega_{ave}$ while the green solid line indicates the Ioffe-Regel limit $1/\omega$ in time, respectively. Phonons exhibit particle-like behavior above the Wigner limit, wave-like behavior between the Wigner limit and the Ioffe-Regel limit, and become overdamped below the Ioffe-Regel limit. c) Energy-dependent particle-like (κ_p) and wave-like (κ_c) spectral thermal conductivities after considering 3+4ph processes at 300 K with their cumulative results along y-direction. d–f) are the anisotropic total thermal conductivity (κ_p+κ_c), including the results of κ_{3ph}+κ_c, κ_{3+4ph}+κ_c, and equilibrium molecular dynamics κ_{EMD} along x-, y- and z-direction. Dashed lines are results from Ref. [27].

spectrum, leading to a pronounced reshaping of the phonon DOS as observed in Figure 3g–i. Figure S7 (Supporting Information) reveals a pronounced asymmetry in Cu's potential energy surface that demands fourth-order polynomial fitting—a clear signature of anharmonicity transcending harmonic description. Consequently, the "beyond rattling" dynamics of Cu ions may induce strong phonon scattering, significantly contributing to the low thermal conductivity.

2.3. Glass-Like Thermal Conductivity

Phonon lifetime analysis further corroborates the extreme anharmonicity. As shown in **Figure** 4a,b, most phonon lifetimes fall within the wave-like tunneling regime, indicating dominant wave-like phonon behavior. Optical modes near 4 meV reside in the overdamped region, especially the results at 600 K. Considering Cu ions do not hop at 300 K, we extract force constants to describe the phonon properties. The calculation provides a clear distribution of phonon lifetimes across the entire phonon energy range. Three-phonon (3ph) scattering confines numerous optical modes to wave-like regions, while higher-energy optical modes exhibit overdamping. Crucially, incorporating four-phonon (4ph) scattering significantly reduces phonon lifetimes, shifting more 4 meV modes into the overdamped regime at 600 K. Notably, the phonon lifetime at 600 K provides a reference for estimating overdamping at elevated temperatures, as Cu ion hopping invalidates the Wigner formulation[26] for precise lifetime predictions under these conditions.

Table S5 (Supporting Information) lists the group velocities of $CsCu_2I_3$ from IXS. The value (≈2.63 km s^{-1}) along Γ−Y direction is relatively higher compared to systems with ultralow particle-like thermal conductivity (κ_p), such as ≈1.36, ≈1.06, and ≈ 1.32 km s^{-1} of $CsPbBr_3$,[28] $CsSnI_3$,[29] and Tl_3VSe_4,[30] respectively. Despite this, extreme anharmonicity suppresses κ_p to extremely low values: ≈0.05, ≈0.03, and ≈0.13 W m^{-1} K^{-1} along x-, y-, and z-directions at 300 K, respectively (Figure 4c; Figure S8, Supporting Information), confirming that anharmonicity, not group velocity, controls thermal transport in $CsCu_2I_3$. Consequently, wave-like thermal conductivity (κ_c) dominates with Cu-related 4 meV modes shown in Figure S6a (Supporting Information) contributing ≈63% of κ_c, similar as that along x- and z-directions.

The hopping motion of Cu ions, particularly at elevated temperatures, contributes significantly to the glass-like temperature dependence of κ. Initially, we calculated the temperature-dependent thermal conductivity using force constants fixed at 300 K. Under this approximation, κ_{3ph}+κ_c decreases with increasing temperature along all three directions. Nevertheless, the temperature dependence is notably weaker than the conventional

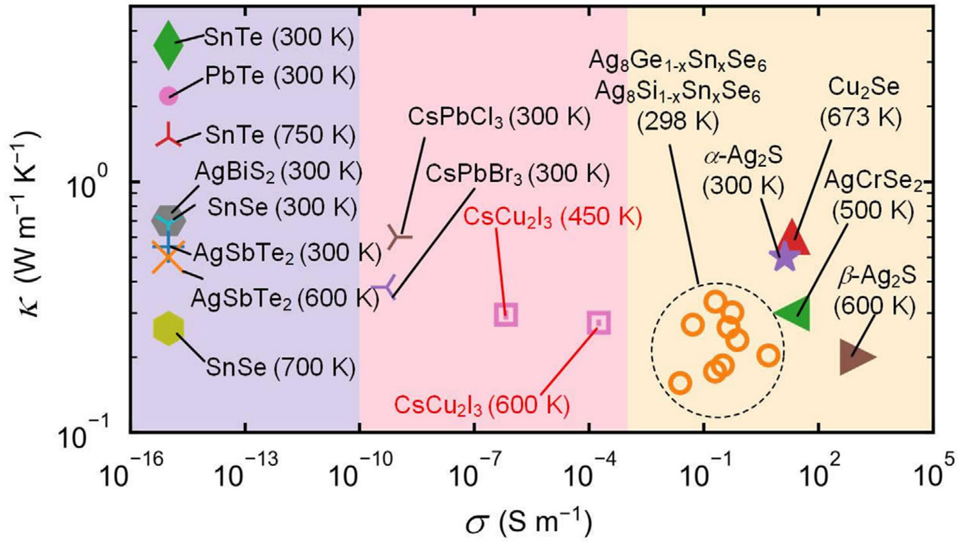

Figure 5. Comparison of ionic transport and thermal conductivity between typical conductors, showing no direct relationship between ionic and phonon conductivity. Light blue, pink, and green shadows indicate the electronic, incipient, and superionic conductors. The average thermal conductivity of $CsCu_2I_3$ is calculated by $(\kappa_x + \kappa_y + \kappa_z)/3$. Other Data are from refs.[11,31–43] Here, an ionic mobility (σ) of 1×10^{-16} S m^{-1} suggests no ionic conduction.

$\kappa \propto T^{-1}$ scaling predicted by dominant 3ph scattering. Specifically, we find $\kappa_x \propto T^{-0.14}$, $\kappa_y \propto T^{-0.31}$, and $\kappa_z \propto T^{-0.49}$ (Figure 4d–f). Inclusion of 4ph process reveals anomalous, glass-like thermal conductivity behavior (κ increasing with T) along the x- and y-directions, characterized by $\kappa_x \propto T^{0.44}$ and $\kappa_y \propto T^{0.66}$. For comparison, Zheng et al. employed the self-consistent phonon approximation to include temperature effects on force constants, and also reported the glass-like behavior along y-direction ($\kappa_y \propto T^{0.13}$), albeit with a weaker relationship than our prediction. In contrast, considering 4ph, our result of $\kappa_z \propto T^{-0.3}$ closely matches Zheng et al.s' of $\kappa_z \propto T^{-0.28}$, suggesting negligible impact of higher-order phonon interactions on κ_c along the z-direction. However, 4ph significantly reduces the magnitude of κ_p, causing an apparent decrease of ≈33%. Additionally, as shown in Figure S9 (Supporting Information), the 4–6 meV optical modes (approximately branches 4–13), strongly influenced by Cu ion motion, contribute 34% to κ_y, whereas the acoustic branches contribute only 17%. This further highlights the significant role of Cu ion dynamics in thermal transport. At higher temperatures, where Cu ion hopping becomes prominent, phonon lifetime enters the overdamped regime, rendering the standard phonon gas model invalid. Therefore, we employed equilibrium molecular dynamics (EMD) simulations combined with the Green-Kubo method to obtain a more comprehensive description of κ (Figure 4d–f), which includes all order phonon interactions. EMD results show $\kappa_x \propto T^{0.17}$, consistent with the highest Cu ionic diffusivity along the x-direction. However, κ_y and κ_z still exhibit decreasing trends ($\kappa_y \propto T^{-0.3}$ and $\kappa_z \propto T^{-0.43}$), differing from the predictions of κ_{3+4ph}+κ_c.

Analysis of the contributions reveals that vibrational transport (κ_V) dominates the total thermal conductivity (Figure S10, Supporting Information). Crucially, the cross-interaction between ionic migration and atomic vibrational (κ_{CROSS}) along the x-direction drives the observed glass-like behavior, while κ_V itself shows only weak temperature dependence. This indicates that in incipient ionic conductors like this, glass-like κ is likely to emerge along the direction of facile ion transport, with κ_{CROSS} being the primary contributor to the positive temperature dependence. Collectively, these findings underscore the critical role of Cu ion hopping in inducing glass-like κ.

Ionic transport contributes to the glass-like κ of $CsCu_2I_3$, yet the average κ maintains a consistent magnitude (≈0.27– ≈0.31 W m^{-1} K^{-1}) (**Figure 5**). Despite significantly enhanced ionic conductivity at elevated temperatures, the minimal κ variation confirms that this ultra-low κ stems primarily from extreme anharmonicity induced by ionic vibrations rather than ionic mobility. Figure 5 summarizes the ionic transport and thermal conductivity between typical conductors. We also present a direct comparison in Table S6 (Supporting Information). In electronic conductors with negligible ionic conductivity (e.g., SnTe[31] and PbTe[32] at 300 K), thermal conductivity is generally higher than that of incipient and superionic conductors and superionic conductors. This is primarily due to the limited phonon anharmonicity (including phonon softening and broadening) induced by atomic vibrations. In superionic conductors (e.g., $CuCrSe_2$[5] and $AgCrSe_2$[10]), long-range ionic migration can selectively disrupt transverse phonon modes, readily causing material degradation despite being glass-like κ. However, when ions migrate with only short-range displacement, such as in $CsCu_2I_3$ and $Cu_{12}Sb_4S_{13}$,[8] giant or extreme anharmonicity beyond rattling occurs in systems, also yielding glassy-κ. As shown in Table S6 (Supporting Information), at 600 K, β-Ag_2S demonstrates characteristic superionic behavior with an exceptionally high electrical conductivity of 1048 S·m^{-1},[33] exceeding that of $CsCu_2I_3$ (1.77×10^{-5} S·m^{-1})[13] by approximately eight orders of magnitude. Remarkably, despite this dramatic difference in ionic conduction properties, both materials exhibit similarly exceptionally low thermal conductivities: 0.27 W m^{-1} K^{-1} for $CsCu_2I_3$ versus 0.20 W m^{-1} K^{-1} for β-Ag_2S,[33] with a small difference of only 0.07 W m^{-1} K^{-1}. Notably, high temperature-enhanced anharmonicity can further reduce thermal conductivity of electronic conductors (e.g., SnSe at 750 K[31] in Figure 5), bringing their κ down to levels comparable with incipient and superionic conductors. This demonstrates that high ionic conductivity is not a prerequisite for achieving ultralow κ. In summary, incipient ionic conductors exhibit anharmonicity levels comparable to superionic conductors while maintaining better stability. Moreover, unlike electronic conductors, they retain remarkably low thermal conductivity across a broad moderate temperature range.

3. Conclusion

This work identifies $CsCu_2I_3$ as a new incipient ionic conductor. Single crystal synchrotron X-ray diffraction combined with MEM analysis reveals the constrained migration of Cu ions, which preferentially undergo nearest-neighbor exchange between CuI_4 tetrahedra along the MID pathway at elevated temperatures. Machine-learning potential-based MD further confirms that this limited migration occurs predominantly along the x-direction via the MID pathway. Although Cu ion migration does not disrupt TA modes, the unique "beyond rattling" behavior of Cu ions induces extreme anharmonicity. The motion of Cu ions significantly contributes to the overdamped optical modes observed in IXS measurements. Phonon modes associated with Cu motion display a distinct propagating character. Furthermore, the mobile Cu ions at high temperatures induce glass-like thermal conductivity by facilitating strong cross-coupling between vibrational (phonon) and ionic-convective heat transport. However, the contribution of mobile Cu ions to the overall change in thermal conductivity is limited. These results propose the Cu/Ag alkali-metal halides as new promising incipient ionic conductors to simultaneously maintain both glassy κ and high stability, reveal the thermal transport mechanism via ion migration constraints, and pave an effective pathway toward significantly low thermal conductivity in ionic conductors.

4. Experimental Section

Sample Synthesis: The single crystal $CsCu_2I_3$ was grown by the modified inverse temperature crystallization method, as shown in our previous work.[44] CsI and CuI in a 1:2 molar ratio were fully dissolved in an OA/DMF (0.8 mL/5 mL) solvent mixture with vigorous stirring for half an hour at room temperature under ambient conditions. In order to remove undesirably undissolved precursors or contaminants, then the resultant greenish solution was filtered into a glass vial using a 0.22 µm poly(tetrafluoroethylene) (PTFE) filter. After that, we quickly sealed the glass vial with a cover and placed it in an oil bath. The heating rate was set as 2 °C h^{-1} until the dark brown solution crystallized one or two small $CsCu_2I_3$ seeds in the vials (75 °C). Afterward, the temperature was maintained at 75 °C to promote the continuous growth of $CsCu_2I_3$ seeds for 72 h.

Single-Crystal Synchrotron X-Ray Diffraction: The high-resolution single-crystal synchrotron X-ray diffraction was conducted at BL02B1 in SPring-8.[45] The photon energy of 50.00 keV with a Pilatus3 X CdTe (P3) detector was utilized, which has recently been regarded as a good tool to achieve extremely high quality for the electron density data.[46] The experiment was conducted at 100, 200, 300, 400, and 500 K with wavelengths of 0.2481 Å. The CrysAlisPro[47] was used to convert the collected frames into Esperanto format and then output the reconstructed files. This reconstruction included the application of an absorption correction using the SCALE3 ABSPACK scaling algorithm. Unwrapped images, as shown in Figure S1 (Supporting Information) were also based on the CrysAlisPro. The refinement was performed in Olex2,[48] where the structures were solved with ShlexT.[49] The detailed structure refinement was conducted by Jana2020.[50] Details of the single-crystal diffraction are shown in Tables S1–S3 (Supporting Information). The high-quality single crystal synchrotron data provide confidence for the next MEM density analysis.

MEM Density Analysis: The structure factors were extracted from the refined high-quality SCSXRD data by Jana2020[50] and then output the file for MEM density analysis with Dysnomia.[51] The Limited-memory BFGS (L-BFGS) algorithm implemented in Dysnomia was chosen for the calculations. The conventional cell of $CsCu_2I_3$ was divided into pixels with a resolution ≈0.05 Å. The entropy was defined as $S = -\sum_{k=1}^{N} \rho_k \ln(\frac{\rho_k}{\tau_k})$, where ρ_k was the normalized density at position in 3D gridded space, and τ_k is the normalized density derived from prior information.[51] A linear combination of generalized constraints with weightings was chosen to maximize entropy S. The constraints C can be described as[51]

$$\begin{aligned} C &= \sum_n \lambda_n C_n \\ C_n &= \frac{1}{(N_F+N_G) M_n(\text{Gauss})} \left[\sum_{j=1}^{N_F} \omega_j \left(\left| \Delta F_j \right| \right)^n + \sum_{j=1}^{G_F} \omega_j \left(\left| \Delta G_j \right| \right)^n \right] - C_{w_n} \end{aligned} \tag{1}$$

where the λ_n is the relative weight of C_n. The ω_j was the weighting factor and C_{wn} was the criterion for convergence. The ΔF_j and ΔG_j are F and G constrain, respectively. M_n was nth order central moment of Gaussian distribution. The MEM calculation results were shown in Table S4 (Supporting Information).

Inelastic X-Ray Scattering: The BL43LXU beamline at SPring-8 was chosen to conduct inelastic X-ray scattering measurements, where 21.7 keV incident energy at 300, 450, and 600 K. The measurements were performed with a resolution of ≈1.5 meV (with analyzer-specific resolutions between 1.427 and 1.709 meV) and a momentum resolution of 0.05 with units of reciprocal lattice (2π/a). The (010) surface of a high-quality $CsCu_2I_3$ single crystal, ≈8 × 1 mm in size, as shown in Figure S11 (Supporting Information), was oriented perpendicular to the X-ray beam. The (7, 7, 0), (0,8,0), (4, 4, 0), and (6, 6, 0) zones were chosen to measure the phonon information. The dynamical structure factor $S(\mathrm{Q}, E)$ was calculated to guide us design the experiment, which could be described as[52,53]

$$\begin{aligned} S(\boldsymbol{Q}, E) \propto \Sigma_s \Sigma_\tau \frac{1}{\omega_\mathrm{s}} \left| \Sigma_d \frac{f_d(\boldsymbol{Q})}{\sqrt{M_\mathrm{d}}} \exp(-W_d) \exp(\mathrm{i}\boldsymbol{Q} \cdot \boldsymbol{r}_d) (\boldsymbol{Q} \cdot \boldsymbol{e}_{ds}) \right|^2 \\ \times \langle \mathrm{n}_s + 1 \rangle \, \delta(\omega - \omega_\mathrm{s}) \, \delta(\boldsymbol{Q} - \boldsymbol{q} - \boldsymbol{\tau}) \end{aligned} \tag{2}$$

where $f_d(\boldsymbol{Q})$ is X-ray form factor of atom d. $\mathbf{Q} = \boldsymbol{k}_f \_ \boldsymbol{k}_i$ indicates the wave vector transfer, where $\boldsymbol{k}_f$ and $\boldsymbol{k}_i$ were the final and incident wave vectors of the scattered particle. $\mathbf{q}$ was the phonon wave vector, ω_s was the eigenvalue of the phonon corresponding to the branch index s, $\boldsymbol{\tau}$ was the reciprocal lattice vector, d was the atom index in the unit cell, $\mathbf{r}_d$ the atom position, W_d was the corresponding Debye-Waller factor, $\mathbf{e}_{ds}$ were the phonon eigenvectors. The second-order force constants at 300 K, which were described as in Machine-learning potential-based calculation method part, were used to obtain $S(\mathbf{Q}, E)$. In order to acquire the phonon shift and phonon linewidth, the damped harmonic oscillator (DHO) model convoluted with the resolution function was applied[54]

$$I(E) = R * \left(A \frac{4\gamma E}{n(E)\,\pi} \frac{1}{\left(E^2 - E_C{}^2\right)^2 + (2\gamma E)^2} \right) \tag{3}$$

where E_c, 2γ, $n(E)$ and A were effective energy of the mode, phonon linewidth (full-width at half-maximum), Bose-Einstein distribution function at phonon energy transfer $E[n(E) = (e^{E/k_BT} - 1)^{-1}]$ and amplitude, respectively.

First-Principles Calculations: First-principles calculations were conducted with Vienna Ab initio Simulation Package (VASP).[55] The exchange-correlation function PBEsol was chosen to relax the lattice, with kinetic energy cutoff 700 eV and electronic energy tolerance 10^{-6} eV. The K-points were chosen as $6 \times 6 \times 8$. The acquired lattice constants $a = 10.04$ Å, $b = 12.94$ Å, and $c = 6.05$ Å are close to the experimental $a = 10.48$ Å, $b = 13.04$ Å, and $c = 6.06$ Å at 100 K.

Machine-Learning Potential Based Calculation: The machine learning interaction potential moment tensor potential (MTP) developed by Shapeev et al.[56] was chosen to conduct a molecular dynamics (MD) simulation. Ab initio molecular dynamics calculations were performed with $2 \times 2 \times 2$ supercell of the primitive cell at 300, 450, and 600 K to provide the training database. In this process, the volume was also scaled, range from 0.95 to 1.05 at 300, 450, and 600 K to provide more configurations for MTP training. The energy cutoff and energy tolerance were set as 600 eV and 10^{-6} eV, respectively. The force tolerance was set as 10^{-3} eV Å^{-1}. The K-point was set as Γ-only. We chose the exchange-correlation function PBEsol to run each simulation for 1200 steps with a timestep of 1 fs/step, with a Nosé-Hoover thermostat controlling temperature. The 3486 configurations were chosen as training data to train MTP with a maximum level of 22. The minimum and maximum cutoff radii for the MTP were chosen to be 2.13 and 7 Å. The fitting weights of energies, forces, and stresses were set as 1, 0.1, and 0.01 in the training processes, respectively. After that, we conducted the active learning strategy based on the D-optimality,[57] as included in the MLIP package, to improve the performance of MTP potential. The break threshold (γ_{break}) and selection threshold (γ_{select}) were set as 10 and 3. New configurations were selected after an independent MD simulation, and then we performed first-principles calculations for these new structures. These configurations were then added to retrain the MTP potential. 13 iterations were performed, and a total of 86 configurations were actively selected. For active learning, the MD simulation was run for 1 ns. The validation of energy and force is shown in Figure S12 (Supporting Information).

MD was conducted with LAMMPS[58] at 300, 450, and 600 K with the $3 \times 3 \times 5$ supercell of the conventional cell. All systems were equilibrated for 2 ns with *NVT* ensemble and then were switched to *NVE* ensemble to collect data for 2 ns. Each step was set as 2 fs in all simulations. The 200 configurations at 300 K were selected to extract the force constants by HIPHIVE.[59] The second, third, and fourth order cutoff distances were set as 8, 6, and 5.2 Å, respectively, which converged as shown in FigureS13a–c (Supporting Information). These force constants were used to calculate the thermal conductivity by FOURPHONON[60,61] with a converged q-mesh $13 \times 13 \times 13$ as shown in Figure S12d (Supporting Information).

The lattice thermal conductivity κ_{L} computed using the Wigner formalism for thermal transport in solids, expressed as $\kappa_{\text{L}} = \kappa_p + \kappa_c$, where κ_p and κ_c represent the particle-like and wave-like contributions to the lattice thermal conductivity, respectively.[26,42] Here, α and β denote Cartesian directions. The particle-like contribution, corresponding to the diagonal terms ($s = s$') of the Wigner heat-flux operator, was given by:[42]

$$\kappa_p^{\alpha\beta} = \frac{1}{VN_{\mathbf{q}}} \sum_{\mathbf{q}s} C_{\mathbf{q},s} v^{\alpha}_{\mathbf{q},s} v^{\beta}_{\mathbf{q},s} \tau_{\mathbf{q},s} \tag{4}$$

where q and s represent the wave vector and band index, respectively; V is the unit cell volume; $N_{\mathbf{q}}$ is the number of sampled **q**-points; and $C_{\mathbf{q},s}$, $v_{\mathbf{q},s}$, and $\tau_{\mathbf{q},s}$ denote the mode-specific heat capacity, group velocity, and phonon lifetime, respectively. The wave-like (coherence) contribution, arising from the off-diagonal terms ($s \neq s$'), is expressed as:[42]

$$\kappa_c^{\alpha\beta} = \frac{\hbar^2}{k_B T^2 V N_{\mathbf{q}}} \Sigma_{\mathbf{q}} \Sigma_{s \neq s'} \frac{\omega_{\mathbf{q},s} + \omega_{\mathbf{q},s'}}{2} v^{\alpha}_{\mathbf{q},ss'} v^{\beta}_{\mathbf{q},ss'}$$
$$\times \frac{\omega_{\mathbf{q},s} n_{\mathbf{q},s} \left(n_{\mathbf{q},s} + 1\right) + \omega_{\mathbf{q},s'} n_{\mathbf{q},s'} \left(n_{\mathbf{q},s'} + 1\right)}{4\left(\omega_{\mathbf{q},s} - \omega_{\mathbf{q},s'}\right)^2 + \left(\Gamma_{\mathbf{q},s} + \Gamma_{\mathbf{q},s'}\right)^2} \times \left(\Gamma_{\mathbf{q},s} + \Gamma_{\mathbf{q},s'}\right) \tag{5}$$

where $\bar{h}$ is the reduced Planck constant, k_B is the Boltzmann constant, $n = 1/(e^{\frac{\hbar\omega_{\mathbf{q},s}}{k_B T}} - 1)$ was the Bose-Einstein distribution, $\omega_{\mathbf{q},s}$ was the phonon frequency, and $\Gamma_{\mathbf{q},s}$ was the scattering rate. The off-diagonal velocity operator was defined as $v_{\mathbf{q},ss'} = \frac{1}{\omega_{\mathbf{q},s} + \omega_{\mathbf{q},s'}} \langle e_{\mathbf{q},s} | \frac{\partial \mathbf{D}}{\partial \mathbf{q}} | e_{\mathbf{q},s'} \rangle$, where **e** and **D** are the eigenvector and dynamical matrix, respectively.

Considering the migration of cooper ions at high temperature, the velocity of Cs, Cu, and I atoms was extracted from the trajectories to obtain the phonon density states by velocity autocorrelation function, which was described as $PDOS(\omega) = \int \langle \sum_i v_i(t_0) \cdot v_i(t_0 + t) \rangle / \langle \sum_i v_i(t_0) \cdot v_i(t_0) \rangle \exp(-2\pi i \omega t) dt$. The t was the correlation time and the <·> indicates the average over all atoms or the same elements.[62] The diffusivity was calculated with $\text{MSD}_{Cu}(t) = 6D_{\text{Cu}}t$, with $6 \times 6 \times 6$ supercells of the conventional cell.[20] All systems were still equilibrated for 2 ns with *NVT* ensemble and then were switched to *NVE* ensemble for 2 ns, with timestep 1 fs. The dynamical structure factor was calculated from trajectories by

$$S(\mathbf{Q}, \omega) = \int \langle \hat{\rho}(\mathbf{r}, t) \hat{\rho}(0, 0) \rangle \exp(-i(\mathbf{Q} \cdot \mathbf{r} - \omega t)) dt d\mathbf{r}$$
$$\equiv \int G(\mathbf{r}, t) \exp(-i(\mathbf{Q} \cdot \mathbf{r} - \omega t)) dt d\mathbf{r} \tag{6}$$

where $\hat{\rho}(\mathbf{r}, t)$ is the quantum mechanical density operator. $G(\mathbf{r},t)$ is regarded as Von-Hove function and the dynamical structure factor is its time- and space- Fourier transformation.[53,63] The $G(\mathbf{r},t)$ can be described as $G(\mathbf{r}, t) = \Sigma_i^N \Sigma_j^N b_i b_j \int \delta(\mathbf{r} - (\mathbf{r}_{\text{i}}(t + t') - \mathbf{r}_{\text{j}}(t'))) dt'$, where $\mathbf{r}_i(t)$ is the ith atom position at time t. The b_i is the scattering length of ith atom. In these simulations, we used $10 \times 10 \times 10$ supercell of a conventional cell, a total 24 000 atoms. The data collection was conducted with *NVE* ensemble for 300 ps after equilibration with *NVT* ensemble for 50 ps with a timestep 1 fs. We calculated the $S(\mathbf{Q}, \omega)$ at 300 K and 600 K along (7, 7-K, 0), (H, 4, 0), and (0, 8, -2+L). The momentum resolutions based on such a simulation are ≈0.15 Å. The energy resolutions are ≈0.14 meV, as shown in Figure 2e,g, and ≈0.41 meV, as shown in Figure S4 (Supporting Information), respectively.

The thermal conductivity was also calculated by MTP-based EMD, which relies on the Green-Kubo method. The heat flux $\mathbf{J}(t)$ is described as[6]

$$J(t) = \sum_i \mathbf{v}_i \varepsilon_i + \frac{1}{2} \sum_{ij, i \neq j} \mathbf{r}_{ij} \left(\mathbf{F}_{ij} \cdot \mathbf{v}_i \right) \tag{7}$$

where $\mathbf{v}_i$ and ϵ_i were the velocity and energy of the ith atom, respectively. $\mathbf{F}_{ij}$ and $\mathbf{r}_{ij}$ were the force and distance between ith and jth atoms, respectively. The first term in equation 7 was convection heat flux $\mathbf{J}_{\text{conv}}(t)$, which was related to the ionic transport. The second term was conduction heat flux $\mathbf{J}_{\text{virial}}(t)$, which was from the lattice vibrations in solids. The total lattice thermal conductivity κ_{EMD} was expressed as below:[64]

$$\kappa_{\text{EMD}} = \frac{1}{3k_B T^2 V} \left[\int_0^t \langle J_{virial}(0) \cdot J_{virial}(t) \rangle dt + \int_0^t \langle J_{conv}(0) \cdot J_{conv}(t) \rangle dt \right.$$
$$\left. + 2 \int_0^t \langle J_{virial}(0) \cdot J_{conv}(t) \rangle dt \right] \tag{8}$$

The first term in the square bracket was the contribution from atomic vibration κ_{V}. The second term was the contribution from the non-phononic convection of migration atoms κ_{CONV} and the third term was the contribution from the cross interactions between ionic migration and atomic vibrational κ_{CROSS}. The $4 \times 3 \times 5$ supercell of conventional cells was used in all κ_{EMD} calculations. All systems were firstly equilibrated with *NVT* ensemble for 20 ps, and then we collected data with *NVE* ensemble. The data collection for the heat flux calculation was 25 ns with a time step 1 fs, which was separated to 25 iterations.

Supporting Information

Supporting Information is available from the Wiley Online Library or from the author.

Acknowledgements

The authors acknowledge Yuiga Nakamura at BL02B1@SPring-8, Jiesheng Hu, and Zishuo Yao at the School of Chemistry and Chemical Engineering in Beijing Institute of Technology for discussion. The work at Beijing Institute of Technology is supported by the National Key R&D Program of China (2021YFA1400300), the Open Fund of the China Spallation Neutron Source Songshan Lake Science City (KFKT2023A07), and Beijing National Laboratory for Condensed Matter Physics (2023BNLCMPKF003). B.W. acknowledges the financial support from the National Science Foundation of China (12304040) and the GuangDong Basic and Applied Basic Research Foundation (2023A1515110762). The work at Beihang University is supported by the support of National Natural Science Foundation of China (No. 52125205, 52250398, 52192614, and 52203307), the Natural Science Foundation of Beijing Municipality (2222088 and L223006), the Shenzhen Science and Technology Program (Grant No. KQTD20170810105439418), and the Fundamental Research Funds for the Central Universities. The authors also thank Xuzhou B&C Chemical Co., Ltd for providing the photoresist (HTA116, HTA112, B&C Chemicals) used in the work. Part of this research was performed at BL43LXU (proposal No. 2022B1379) and BL02B1 (proposal No. 2023B2064) at the SPring-8, Japan, under a user program. The authors thank the Beijing PARATERA Tech CO., Ltd. https://cloud.paratera.com.

Conflict of Interest

The authors declare no conflict of interest.

Author Contributions

Y.L., B.W., and J.H. designed the project. Y.L., C.L., D.I., T.M., and A.B. carried out the IXS experiment and analyzed the data. Y.L. and J.H. performed the simulation. C.L. and C.P. prepared the single crystal. Y.L., B.W., X.J., and J.H. discussed this work. Y.L. and B.W. wrote the original manuscript. C.P. and J.H. supervised the project. All the authors reviewed and edited the manuscript.

Data Availability Statement

All data related to the conclusion are present in the paper and the Supporting Information. The information of material structure, force constants, and thermal conductivity tensor can be found in https://github.com/davy12344/Thermal-transport-and-Machine-learning-potential. The data related to this paper can be requested from the authors.

Keywords

inelastic experiment, ionic conductor, phonon, thermal conductivity

Received: July 13, 2025
Revised: August 18, 2025
Published online:

[1] X. Shi, J. Yang, J. R. Salvador, M. Chi, J. Y. Cho, H. Wang, S. Bai, J. Yang, W. Zhang, L. Chen, *J. Am. Chem. Soc.* **2011**, *133*, 7837.
[2] B. C. Sales, B. C. Chakoumakos, D. Mandrus, J. W. Sharp, *J. Solid State Chem.* **1999**, *146*, 528.
[3] J. L. Cohn, G. S. Nolas, V. Fessatidis, T. H. Metcalf, G. A. Slack, *Phys. Rev. Lett.* **1999**, *82*, 779.
[4] H. Hu, Y. Ju, J. Yu, Z. Wang, J. Pei, H.-C. Thong, J.-W. Li, B. Cai, F. Liu, Z. Han, B. Su, H.-L. Zhuang, Y. Jiang, H. Li, Q. Li, H. Zhao, B.-P. Zhang, J. Zhu, J.-F. Li, *Nat. Mater.* **2024**, *23*, 527.
[5] J. L. Niedziela, D. Bansal, A. F. May, J. Ding, T. Lanigan-Atkins, G. Ehlers, D. L. Abernathy, A. Said, O. Delaire, *Nat. Phys.* **2019**, *15*, 73.
[6] Q. Ren, M. K. Gupta, M. Jin, J. Ding, J. Wu, Z. Chen, S. Lin, O. Fabelo, J. A. Rodríguez-Velamazán, M. Kofu, K. Nakajima, M. Wolf, F. Zhu, J. Wang, Z. Cheng, G. Wang, X. Tong, Y. Pei, O. Delaire, J. Ma, *Nat. Mater.* **2023**, *22*, 999.
[7] K. Zhao, P. Qiu, X. Shi, L. Chen, *Adv. Funct. Mater.* **2020**, *30*, 1903867.
[8] S. Mukherjee, D. J. Voneshen, A. Duff, P. Goddard, A. V. Powell, P. Vaqueiro, *Adv. Mater.* **2023**, *35*, 2306088.
[9] K. S. Rana, Nidhi, C. B., K. Biswas, A. Soni, *J. Mater. Chem. A* **2024**, *12*, 22756.
[10] J. Ding, J. L. Niedziela, D. Bansal, J. Wang, X. He, A. F. May, G. Ehlers, D. L. Abernathy, A. Said, A. Alatas, Y. Ren, G. Arya, O. Delaire, *Science* **2020**, *117*, 3930.
[11] T. Bernges, R. Hanus, B. Wankmiller, K. Imasato, S. Lin, M. Ghidiu, M. Gerlitz, M. Peterlechner, S. Graham, G. Hautier, Y. Pei, M. R. Hansen, G. Wilde, G. J. Snyder, J. George, M. T. Agne, W. G. Zeier, *Adv. Energy Mater.* **2022**, *12*, 2200717.
[12] J. W. Park, Y.-K. Jung, A. Walsh, *P. R. X. Energy* **2023**, *2*, 043004.
[13] S. Hull, P. Berastegui, *J. Solid State Chem.* **2004**, *177*, 3156.
[14] D. M. Collins, *Nature* **1982**, *298*, 49.
[15] B. Iversen, F. Larsen, M. Souhassou, M. Takata, *Acta Crystallogr. Sect. B: Struct. Sci* **1995**, *51*, 580.
[16] M. Takata, B. Umeda, E. Nishibori, M. Sakata, Y. Saitot, M. Ohno, H. Shinohara, *Nature* **1995**, *377*, 46.
[17] S. Kastbjerg, N. Bindzus, M. Søndergaard, S. Johnsen, N. Lock, M. Christensen, M. Takata, M. A. Spackman, B. B. Iversen, *Adv. Funct. Mater.* **2013**, *23*, 5477.
[18] J. Zhang, N. Roth, K. Tolborg, S. Takahashi, L. Song, M. Bondesgaard, E. Nishibori, B. B. Iversen, *Nat. Commun.* **2021**, *12*, 6709.
[19] S. Nishimura, G. Kobayashi, K. Ohoyama, R. Kanno, M. Yashima, A. Yamada, *Nat. Mater.* **2008**, *7*, 707.
[20] C. Wang, Y. Chen, *Nano Lett.* **2023**, *23*, 3524.
[21] M. K. Gupta, J. Ding, D. Bansal, D. L. Abernathy, G. Ehlers, N. C. Osti, W. G. Zeier, O. Delaire, *Adv. Energy Mater.* **2022**, *12*, 2200596.
[22] A. Q. R. Baron, *SPring-8 Inf. Newsl.* **2010**, *15*, 14.
[23] A. Q. R. Baron, in Synchrotron Light Sources and Free-Electron Lasers, Springer, Cham, **2016**, pp. 1643–1719.
[24] A. Q. R. Baron, **2020**, https://doi.org/10.48550/arXiv.1504.01098.
[25] D. J. Voneshen, H. C. Walker, K. Refson, J. P. Goff, *Phys. Rev. Lett.* **2017**, *118*, 145901.
[26] M. Simoncelli, N. Marzari, F. Mauri, *Phys. Rev. X* **2022**, *12*, 041011.
[27] J. Zheng, C. Lin, C. Lin, B. Huang, R. Guo, G. Hautier, *arXiv* **2023**, https://doi.org/10.48550/arXiv.2310.13680.
[28] H. Xie, S. Hao, J. Bao, T. J. Slade, G. J. Snyder, C. Wolverton, M. G. Kanatzidis, *J. Am. Chem. Soc.* **2020**, *142*, 9553.
[29] G. A. Elbaz, W.-L. Ong, E. A. Doud, P. Kim, D. W. Paley, X. Roy, J. A. Malen, *Nano Lett.* **2017**, *17*, 5734.
[30] S. Mukhopadhyay, D. S. Parker, B. C. Sales, A. A. Puretzky, M. A. McGuire, L. Lindsay, *Science* **2018**, *360*, 1455.
[31] L.-D. Zhao, S.-H. Lo, Y. Zhang, H. Sun, G. Tan, C. Uher, C. Wolverton, V. P. Dravid, M. G. Kanatzidis, *Nature* **2014**, *508*, 373.
[32] Y. Xia, *Appl. Phys. Lett.* **2018**, *113*, 073901.
[33] Tuo W., Hong-Yi C., Peng-Fei Q., Xun S., Li-Dong C., *Acta Phys. Sin.* **2019**, *68*, 090201.
[34] S. Roychowdhury, T. Ghosh, R. Arora, M. Samanta, L. Xie, N. K. Singh, A. Soni, J. He, U. V. Waghmare, K. Biswas, *Science* **2021**, *371*, 722.
[35] S. Roychowdhury, T. Ghosh, R. Arora, U. V. Waghmare, K. Biswas, *Angew. Chem.* **2018**, *130*, 15387.
[36] T. Fu, J. Xin, T. Zhu, J. Shen, T. Fang, X. Zhao, *Sci. Bull* **2019**, *64*, 1024.
[37] B. A. Boukamp, G. A. Wiegers, *Solid State Ion* **1983**, *9–10*, 1193.
[38] K. S. Rana, A. Singh, A. Bhui, K. Biswas, A. Soni, *ACS Appl. Energy Mater.* **2024**, *7*, 5621.

[39] D. Yang, X. Su, J. Li, H. Bai, S. Wang, Z. Li, H. Tang, K. Tang, T. Luo, Y. Yan, J. Wu, J. Yang, Q. Zhang, C. Uher, M. G. Kanatzidis, X. Tang, *Adv. Mater.* **2020**, *32*, 2003730.
[40] D. Pushcharovsky, A. Ivanov-Schitz, *Minerals* **2024**, *14*, 770.
[41] R. L. Narayan, M. V. S. Sarma, S. V. Suryanarayana, *J. Mater. Sci. Lett.* **1987**, *6*, 93.
[42] M. Simoncelli, N. Marzari, F. Mauri, *Nat. Phys.* **2019**, *15*, 809.
[43] Y. He, C. C. Stoumpos, I. Hadar, Z. Luo, K. M. McCall, Z. Liu, D. Y. Chung, B. W. Wessels, M. G. Kanatzidis, *J. Am. Chem. Soc.* **2021**, *143*, 2068.
[44] X. Mo, T. Li, F. Huang, Z. Li, Y. Zhou, T. Lin, Y. Ouyang, X. Tao, C. Pan, *Nano Energy* **2021**, *81*, 105570.
[45] K. Sugimoto, H. Ohsumi, S. Aoyagi, E. Nishibori, C. Moriyoshi, Y. Kuroiwa, H. Sawa, M. Takata, *2010* **1234**, 887.
[46] L. Krause, K. Tolborg, T. B. E. Grønbech, K. Sugimoto, B. B. Iversen, J. Overgaard, *J. Appl. Crystallogr.* **2020**, *53*, 635.
[47] Rigaku Oxford Diffraction, CrysAlisPro Software system, version 1.171.39.45f, Rigaku Corporation, Wroclaw, Poland, **2024**.
[48] O. V. Dolomanov, L. J. Bourhis, R. J. Gildea, J. a. K. Howard, H. Puschmann, *J. Appl. Crystallogr.* **2009**, *42*, 339.
[49] G. M. Sheldrick, *Acta Cryst A* **2015**, *71*, 3.
[50] V. Petříček, L. Palatinus, J. Plášil, M. Dušek, Z. Krist-Cryst, *Mater.* **2023**, *238*, 271.
[51] K. Momma, T. Ikeda, A. A. Belik, F. Izumi, *Powder Diffr.* **2013**, *28*, 184.
[52] B. Wei, Q. Cai, Q. Sun, Y. Su, A. H. Said, D. L. Abernathy, J. Hong, C. Li, *Commun. Phys.* **2021**, *4*, 227.
[53] G. L. Squires, *Introduction to the Theory of Thermal Neutron Scattering*, Cambridge University Press, Cambridge, **2012**.
[54] A. Q. R. Baron, *J. Phys. Soc. Jpn.* **2009**, *58*, 205.
[55] G. Sun, J. Kürti, P. Rajczy, M. Kertesz, J. Hafner, G. Kresse, *J. Mol. Struct.* **2003**, *624*, 37.
[56] I. S. Novikov, K. Gubaev, E. V. Podryabinkin, A. V. Shapeev, *Mach. Learn.: Sci. Technol.* **2020**, *2*, 025002.
[57] E. V. Podryabinkin, A. V. Shapeev, *Comput. Mater. Sci.* **2017**, *140*, 171.
[58] A. P. Thompson, H. M. Aktulga, R. Berger, D. S. Bolintineanu, W. M. Brown, P. S. Crozier, P. J. In 't Veld, A. Kohlmeyer, S. G. Moore, T. D. Nguyen, R. Shan, M. J. Stevens, J. Tranchida, C. Trott, S. J. Plimpton, *Comput. Phys. Commun.* **2022**, *271*, 108171.
[59] F. Eriksson, E. Fransson, P. Erhart, *Adv. Theory Simul.* **2019**, *2*, 1800184.
[60] Z. Han, X. Yang, W. Li, T. Feng, X. Ruan, *Comput. Phys. Commun.* **2022**, *270*, 108179.
[61] W. Li, J. Carrete, N. A. Katcho, N. Mingo, *Comput. Phys. Commun.* **2014**, *185*, 1747.
[62] L. T. Kong, J. F. Li, Q. W. Shi, H. J. Huang, K. Zhao, *EPL* **2012**, *97*, 56004.
[63] N. J. Weadock, T. C. Sterling, J. A. Vigil, A. Gold-Parker, I. C. Smith, B. Ahammed, M. J. Krogstad, F. Ye, D. Voneshen, P. M. Gehring, A. M. Rappe, H.-G. Steinrück, E. Ertekin, H. I. Karunadasa, D. Reznik, M. F. Toney, *Joule* **2023**, *7*, 1051.
[64] Y. Zhou, S. Xiong, X. Zhang, S. Volz, M. Hu, *Nat. Commun.* **2018**, *9*, 4712.